Research Article

Humaira Yasmin*, Rawan Bossly, Fuad S. Alduais, Afrah Al-Bossly, and Arshad Khan*

Impacts of double stratification on thermally radiative third-grade nanofluid flow on elongating cylinder with homogeneous/heterogeneous reactions by implementing machine learning approach

https://doi.org/10.1515/ntrev-2025-0199
received December 17, 2024; accepted June 26, 2025

Abstract: This work investigates the influences of double stratification on a thermally radiative third-grade nanofluid flow. The fluid flowed on a stretching cylinder. It is considered that the homogeneous reaction occurs at ambient flow, while the heterogeneous reaction occurs at the wall of the cylinder. The modeled equations were solved using an artificial neural network (ANN) approach. The outcomes of this work revealed that the maximum performance of the modeled problem was obtained at epochs 295, 1,000, 687, and 117 by using an ANN design. The velocity characteristics of the fluid decreased with an increase in the magnetic and curvature factors and increased with an increase in the third-grade dimensionless factor. The temperature distribution diminished with an increase in the curvature factor of the cylinder and thermal stratification factor, and increased with an increase in the radiation factor. The heat transfer field weakened with an increase in the Schmidt number and quotient of the diffusion coefficients and augmented with an increase in the homogeneous/heterogeneous reaction strength factors. The absolute errors are evaluated for all the four scenarios that fall within the range of 10^{-3}–10^{-8} and are associated with the corresponding ANN configuration that demonstrates a fine degree of accuracy.

Keywords: magnetohydrodynamic, nanofluid flow, third-grade fluid, stretching cylinder, homogeneous/heterogeneous reactions, thermal radiations, ANN approach

1 Introduction

Magnetohydrodynamic (MHD) fluid flows are used to study the behavior of electrically conductive fluids by employing magnetic fields. Reddy *et al.* [1] examined that in MHD flows, the collaboration between the magnetic field and the conductive fluid generates a Lorentz force, which influences both the velocity and thermal distributions. Lone *et al.* [2] revealed that in the case of an MHD nanofluid flow on a convective heat sheet, the velocity field was affected because the Lorentz force behaved as an opposite force, decelerating the fluid motion (often referred to as magnetic damping). MHD fluid flow is beneficial in engineering applications, like cooling systems in nuclear reactors or magnetic confinement in fusion reactors, where controlling the fluid's velocity is crucial for efficiency [3,4]. MHD flows influence heat transfer by altering the temperature gradient within the fluid. The magnetic field reduces convective heat transference by impeding fluid motion, which causes more uniform temperature distributions in most scenarios, as perceived by Ahmad *et al.* [5]. Tarakaramu *et al.* [6] inspected computationally convective constraints for the MHD fluid flow using nonlinear thermal radiations and heat absorptions. Rafique *et al.* [7] discussed mathematically and physically the MHD nanofluid flow using slip constraints and variable viscous forces on an elongating sheet. The thermal behavior in the case of MHD fluid flow is

* **Corresponding author: Humaira Yasmin**, Department of Basic Sciences, General Administration of Preparatory Year, King Faisal University, P.O. Box 400, Al Ahsa, 31982, Saudi Arabia; Department of Mathematics and Statistics, College of Science, King Faisal University, P.O. Box 400, Al Ahsa, 31982, Saudi Arabia, e-mail: hhassain@kfu.edu.sa
* **Corresponding author: Arshad Khan**, College of Aeronautical Engineering, National University of Sciences and Technology, Sector H-12, Islamabad, 44000, Pakistan, e-mail: arshad8084@gmail.com
Rawan Bossly: Department of Mathematics, College of Science, Jazan University, Jazan, 82817, Saudi Arabia
Fuad S. Alduais, Afrah Al-Bossly: Department of Mathematics, College of Science and Humanities in Al-Kharj, Prince Sattam bin Abdulaziz University, Al-Kharj, 11942, Saudi Arabia

substantial in applications where heat dissipation needs to be carefully controlled, like in MHD generators or space vehicle cooling systems [8]. Moreover, in some cases, magnetic fields also induce heating through Joule heating, which occurs when the fluid's electrical opposition converts kinetic energy into heat, thereby influencing the thermal distribution in complex ways. The coupling of magnetic fields with conductive fluids in MHD impacts velocity and temperature profiles, with applications across the energy, aerospace, and engineering sectors.

Nanofluid flow describes the study of fluids dispersed in a base fluid. Nanofluids are primarily designed to enhance thermal conductivity, as developed by Choi and Eastman [9]. Al-Essa *et al.* [10] established that nanofluids have higher heat transfer capabilities in comparison to conventional fluids, making them ideal for advanced heat transfer applications in industries like electronics' coolants, biomedical devices, and energy systems. Akbar *et al.* [11] discussed thermal flow augmentation for the trihybrid nanofluid flow and entropy optimization on an extending sheet. Shah *et al.* [12] analyzed the thermal energy using the particle swarm optimization approach for the trihybrid nanofluid flow with an artificial neural network (ANN) approach. In terms of velocity distribution, nanofluids exhibited unique behaviors compared to traditional fluids. Srilatha *et al.* [13] found that the presence of nanoparticles increases the effective viscosity of the fluid, which reduces the velocity of the flow under certain conditions. However, this effect is balanced by the improved thermal properties of the nanofluids. Depending on the nanoparticle concentration and size, nanofluids enhance momentum transport within the fluid, leading to better mixing and potentially higher velocities in some regions of the flow. Akbar *et al.* [14] examined the hybrid boiling nanoliquid flow with convective constraints at the boundary through a permeable elongating channel using the machine learning approach. Regarding temperature distribution, nanofluids dramatically enhance heat transfer due to their improved thermal conductivity. This leads to a more efficient energy transfer process, with nanofluids dissipating heat faster than traditional fluids. As a result, the temperature gradient within the fluid was reduced, leading to more uniform temperature distributions. Shamshuddin *et al.* [15] debated the thermal transmissions for convective magnetized nanofluid flow in a permeable cylindrical annular space. In applications requiring rapid cooling or heating, this characteristic is highly beneficial, like the coolant of heat exchangers and the coolant of electric devices. However, the increased heat transfer capability can also result in localized hotspots if the nanofluid is not properly managed. Li *et al.* [16] examined Jeffery fluid oscillating flow in a circular rough microchannel with slip constraints at the boundary. Alghamdi *et al.* [17] studied mixed convective thermally stratified micropolar nanofluid flow on a heated sheet with thermal diffusion using a machine learning technique. Overall, nanofluids provide a significant enhancement in both velocity and temperature control, which is crucial for high-performance heat exchange systems. Sun *et al.* [18] examined the effects of silica nanocomposites and carbon fibers on the rheological performance of shear-thickening fluids.

Fluid flow on a stretching cylinder is a classical problem in fluid mechanics and is often analyzed in the theory of boundary layers. This scenario typically arises in industrial processes like extrusion, wire drawing, or glass fiber production, where the stretching of cylindrical surfaces affects the flow dynamics. The cylinder's stretching introduces a velocity along its surface, altering the flow characteristics and developing a boundary layer where viscous forces are dominant. Abbas *et al.* [19] examined the time-dependent induced MHD fluid flow on a nonlinear elongating cylinder. Sudarmozhi *et al.* [20] inspected mass and thermal transmissions on a permeable elongating cylinder. In contrast to the flow over a flat plate, the curvature of the cylinder plays a significant role in shaping the boundary layer's width and velocity profiles, as observed by Khan *et al.* [21]. As the fluid flows over the stretching surface, it experiences an increasing radial velocity component due to the stretching, leading to a more complex shear stress distribution than that in a flat geometry. Islam *et al.* [22] observed that several parameters influence the flow behavior, like the Reynolds number and the ratio of stretching velocity to free stream velocity. Sowmiya and Kumar [23] discussed Maxwell and MHD fluid flows on a cylinder with permeable effects and microorganisms. Surface stretching enhances heat and mass transfer, making it essential for engineering applications that require efficient cooling or coating, as observed by Ashraf *et al.* [24]. Asghar *et al.* [25] evaluated dual solutions for the convective spinning fluid flow on a linear shrinking/stretching sheet. Alghamdi *et al.* [26] studied the dual-layer combined convective heated flow on an elevated elongating cylinder using an intelligent computing technique.

Fluid flow involving homogeneous and heterogeneous reactions is imperative in chemical and process engineering, particularly in catalysis, environmental processes, and chemical reactors. In homogeneous reactions, the reactants and products are in the same phase, typically gas or liquid. These reactions occur uniformly throughout the fluid flow, leading to a more predictable and continuous interaction between the reacting species. Madkhali *et al.* [27] inspected computationally the homogeneous and heterogeneous reactions on the fluid flow with transportation mechanisms. Ramzan *et al.* [28] used the impacts of these reactions on a nanofluid flow through a permeable channel using applications of the Das and Tiwari model.

Naseem *et al.* [29] used these reactions for nanoparticle flow on a Riga sheet with impressions of viscous dissipative effects. Homogeneous reactions are influenced by flow dynamics like convection, diffusion, and mixing, which impact reaction rates and product formation [30]. An example is the combustion of gases or the dissolution of a solute in a liquid stream, where the reaction and transport phenomena are tightly coupled. In contrast, heterogeneous reactions involve more than one phase, such as when a solid catalyst interacts with a gas or liquid reactant. Here, the reaction occurs at the interface between the different phases, making surface phenomena like adsorption, desorption, and surface diffusion critical factors in reaction rates. Heterogeneous reactions often dominate processes like catalytic cracking, gas–solid reactions in environmental cleanup, or liquid–solid reactions in industrial chemical synthesis. Jiang *et al.* [31] studied the sharpening-interface algorithm to simulate underwater explosions using multiphase compressible flow on a complex grid. In such cases, the fluid flow is critical because it determines how reactants are transported to and away from the surface of the solid phase. Mass transfer limitations occur, particularly at high flow rates or in systems with low diffusivity, leading to a lower reaction rate at the solid surface compared to what the reaction kinetics would predict under ideal conditions. The interaction between the flow dynamics and reaction kinetics is central to optimizing these systems. Shah *et al.* [32] revealed that factors like flow velocity, temperature, pressure, and concentration gradients must be carefully controlled to ensure maximum efficiency in both homogeneous and heterogeneous reaction-dominated processes, whether in reactors, environmental control systems, or industrial applications.

Fluid flow with thermal radiation is a key aspect in many engineering applications, like high-temperature systems, combustion processes, and astrophysical phenomena. In these systems, thermal radiation plays a substantial role in energy transference alongside convection and conduction, as observed by Kandeal *et al.* [33]. Radiative heat transfer occurs when electromagnetic radiation, typically in the infrared spectrum, is emitted by a hot fluid or surface and absorbed by the surrounding cooler fluid or boundaries. Yang *et al.* [34] examined nano-α′ precipitates effects with dislocation and irradiation effects. Their study enhanced our understanding of irradiation-induced changes in nanostructured materials. Hamad *et al.* [35] revealed that the intensity of thermal radiation depends on factors like temperature, surface emissivity, and the medium's optical properties. Unlike conduction and convection, thermal radiation does not require a medium and can occur across a vacuum or transparent media, making it essential in systems involving high-temperature gradients [36]. Pandey *et al.* [37] highlighted that when fluid flow interacts with thermal radiation, the energy exchange impacts the flow dynamics by altering the temperature distribution within the fluid by augmenting the thermal distribution. For instance, in combustion processes or high-speed aerodynamic flows, thermal radiation can increase the energy content of the flow. The presence of thermal radiation also influences the heat transfer rates significantly, especially in systems with optically thick fluids or gases, where absorption and re-emission of radiation occur frequently [38]. Applications of fluid flow with thermal radiation include cooling systems for electronic devices, nuclear reactors, and solar collectors, where managing heat transfer effectively is critical to system safety and efficiency [39,40].

From the cited literature, it has been revealed that no work has yet been conducted to discuss the impacts of homogenous and heterogeneous reactions on a third-grade fluid past an elongating cylinder using the ANN approach. This creates a gap in the existing literature; to fill this gap, the following assumptions have been considered in the current work:

- Third-grade fluid was placed on a stretching cylinder.
- The impacts of homogeneous and heterogeneous reactions are imposed on the fluid flow.
- The influence of double stratification on a thermally radiative third-grade nanofluid flow was investigated.
- The impacts of thermal radiation and heat sink/source were incorporated into the temperature equations.
- The modeled equations were solved using the ANN approach.

1.1 Practical applications of the problem

This research has significant applications in various engineering and scientific fields. It enhances the heat transfer efficiency in industrial cooling systems, including heat exchangers and microelectronics cooling. In biomedical engineering, it aids in precise temperature control for drug delivery and hyperthermia therapy. The study also supports renewable energy technologies, optimizing solar collectors, and geothermal systems. In the chemical and petrochemical industries, it improves the reaction rates and mixing efficiency in reactors. Additionally, manufacturing processes like polymer extrusion and metal casting gain better temperature control. As an illustration of the domain in an engineering process, this research applies to industrial heat exchangers, where third-grade nanofluids improve the heat transfer. Double stratification affects thermal and mass transfer, while homogeneous and

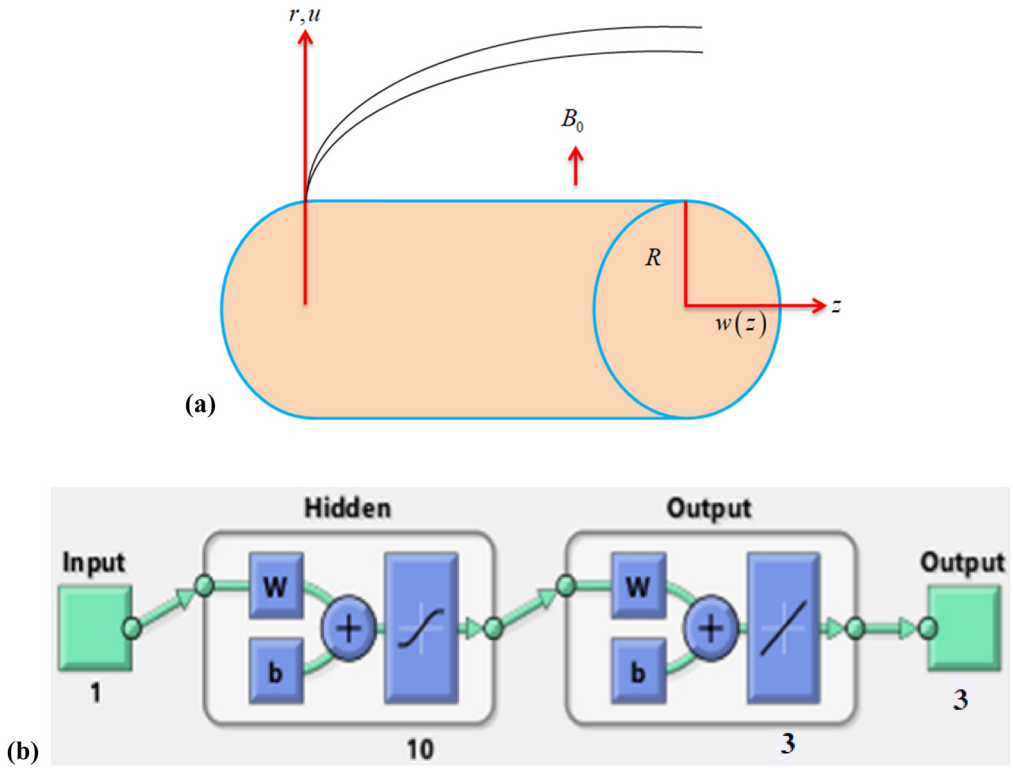

Figure 1: (a): Geometrical situation of the flow problem. (b) Layer dissemination modeled problem using the LMS-NNA design.

heterogeneous reactions refine chemical processes. Thermal radiation influences heat dissipation, and machine learning enhances predictive modeling, optimizing efficiency, process control, and energy savings in manufacturing and chemical industries.

2 Problem formulation

Take a third-grade fluid flow with radiation effects on a stretching cylinder with double stratification. The flow of fluid is bounded by $r > 0$. The cylinder is stretched along the z-axis with velocity $W(z) = W_0 z/l$ with l as the specific length, while r-axis is normal to the flow direction. The fluid is impacted by homogeneous and heterogeneous reactions, thermal radiation, and thermal source/sink effects. The temperatures at the wall of the cylinder and the free stream are depicted as T_w and T_∞, respectively, as shown in Figure 1(a).

Implementing the stated assumptions, we have [41,42]

$$\frac{\partial u}{\partial r} + \frac{u}{r} + \frac{\partial w}{\partial z} = 0, \tag{1}$$

$$\begin{aligned}\rho\left[u\frac{\partial w}{\partial r} + w\frac{\partial w}{\partial z}\right] &= \mu\left[\frac{\partial^2 w}{\partial r^2} + \frac{1}{r}\frac{\partial w}{\partial r}\right] + \beta_3\left[\frac{2}{r}\left(\frac{\partial w}{\partial r}\right)^3 + 6\frac{\partial^2 w}{\partial r^2}\left(\frac{\partial w}{\partial r}\right)^2\right] \\ &+ \alpha_1\left[\begin{array}{l}\frac{w}{r}\left(\frac{\partial^2 w}{\partial r\partial z}\right) + \frac{u}{r}\left(\frac{\partial^2 w}{\partial r^2}\right) + \frac{3}{r}\left(\frac{\partial w}{\partial z}\right)\left(\frac{\partial w}{\partial r}\right) + \frac{1}{r}\left(\frac{\partial u}{\partial r}\right)\left(\frac{\partial w}{\partial r}\right) + 4\left(\frac{\partial^2 w}{\partial r\partial z}\right)\left(\frac{\partial w}{\partial r}\right) \\ + w\frac{\partial^3 w}{\partial r^2\partial z} + 2\left(\frac{\partial^2 w}{\partial r^2}\right)\left(\frac{\partial u}{\partial r}\right) + u\left(\frac{\partial^3 w}{\partial r^3}\right) + 3\left(\frac{\partial^2 w}{\partial r^2}\right)\left(\frac{\partial w}{\partial z}\right) + \left(\frac{\partial^2 u}{\partial r^2}\right)\left(\frac{\partial w}{\partial r}\right)\end{array}\right] \\ &+ \alpha_2\left[\begin{array}{l}\frac{2}{r}\left(\frac{\partial u}{\partial r}\right)\left(\frac{\partial w}{\partial r}\right) + \frac{z}{r}\left(\frac{\partial w}{\partial z}\right)\left(\frac{\partial w}{\partial r}\right) + 2\left(\frac{\partial w}{\partial r}\right)\left(\frac{\partial^2 u}{\partial r^2}\right) \\ + 2\left(\frac{\partial u}{\partial r}\right)\left(\frac{\partial^2 w}{\partial r^2}\right) + 2\left(\frac{\partial w}{\partial z}\right)\left(\frac{\partial^2 w}{\partial r^2}\right) + 4\left(\frac{\partial^2 w}{\partial r\partial z}\right)\left(\frac{\partial w}{\partial r}\right)\end{array}\right] - \frac{\sigma {B_0}^2}{\rho}(w - w_e),\end{aligned} \tag{2}$$

$$u\frac{\partial T}{\partial r} + w\frac{\partial T}{\partial z} = \frac{k}{\rho c_p}\left[\frac{\partial^2 T}{\partial r^2} + \frac{1}{r}\frac{\partial T}{\partial r}\right] - \frac{1}{\rho c_p}\frac{1}{r}\frac{\partial (r q_r)}{\partial r} + \frac{Q_0}{\rho c_p}(T - T_\infty), \tag{3}$$

$$u\frac{\partial a}{\partial r} + w\frac{\partial a}{\partial z} = D_A\left[\frac{\partial^2 a}{\partial r^2} + \frac{1}{r}\frac{\partial a}{\partial r}\right] - k_c a b^2, \tag{4}$$

$$u\frac{\partial b}{\partial r} + w\frac{\partial b}{\partial z} = D_B\left[\frac{\partial^2 b}{\partial r^2} + \frac{1}{r}\frac{\partial b}{\partial r}\right] - k_c a b^2. \tag{5}$$

The boundary conditions for the current flow problem are based on physical constraints at the cylinder's surface and in the far field. The thermal boundary conditions account for the temperature variation due to thermal stratification and radiation, with the surface temperature set as T_w and the ambient temperature approaching T_∞. The subjected boundary conditions are [41,42] as follows:

$$\begin{aligned} &W(r,z) = \frac{W_0 z}{l}, u(r,z) = 0, T = T_w, \\ &D_B\frac{\partial b}{\partial r} = -k_s a, D_A\frac{\partial a}{\partial r} = k_s a, \quad \text{at} \quad r = R, \\ &W(r,z) = 0, T = T_\infty, a = a_0, b = b_0 \quad \text{as} \quad r \to \infty. \end{aligned} \tag{6}$$

Here, u, w are the flow components in the z and r directions, D_A and D_B are the diffusion coefficients of species A and B, $W(r, z) = W_0 z/l$ shows the velocity with which the cylinder is stretched, and Q_0 is a factor for heat generation (when $Q_0 > 0$) and absorption ($Q_0 < 0$). The value of q_r is given by

$$q_r = -\frac{4}{3}\frac{\sigma^*}{k^*}\frac{\partial T^4}{\partial z}. \tag{7}$$

With the help of equation (7), equation (3) becomes

$$u\frac{\partial T}{\partial r} + w\frac{\partial T}{\partial z} = \frac{k}{\rho c_p}\left[\frac{\partial^2 T}{\partial r^2} + \frac{1}{r}\frac{\partial T}{\partial r}\right] + \frac{1}{\rho c_p}\frac{1}{r}\frac{4\sigma^*}{3k^*}\frac{\partial}{\partial r}\left(r\frac{\partial T^4}{\partial r}\right) + \frac{Q_0}{\rho c_p}(T - T_\infty). \tag{8}$$

The variables for transformation are [41,42]

$$\begin{aligned} &w(r,z) = f'(\eta)\frac{W_0 z}{l}, u(r,z) = -\left(\frac{\nu W_0}{l}\right)^{1/2}\frac{R}{r}f(\eta), \\ &\eta = \left(\frac{W_0}{\nu l}\right)^{1/2}\frac{(r^2 - R^2)}{2R}, \\ &\theta(\eta) = \frac{T - T_\infty}{T_w - T_\infty}, a = a_0 \quad \phi(\eta), \quad b = a_0 h(\eta). \end{aligned} \tag{9}$$

Making use of equation (9), we have

$$\begin{aligned} &(1 + 2\eta\gamma)f''' + 2\gamma f + ff'' - (f')^2 \\ &+ \alpha_1[(1 + 2\gamma\eta)\{3f''^2 + 2f'''f' - f^{(iv)}f\} \\ &- \gamma(2f'''f - 6f''f')] \\ &+ \alpha_2[2(1 + 2\gamma\eta)f''^2 + 2\gamma(ff''' + f''f')] \\ &+ \mathrm{Re}\beta[6(1 + 2\gamma\eta)^2 f'''f''^2 + 8\gamma(1 + 2\gamma\eta)f''^2] \\ &- M(f' - 1) = 0, \end{aligned} \tag{10}$$

$$(1 + 2\gamma\eta)\left(1 + \frac{4}{3}\mathrm{Rd}\right)\theta'' + 2\gamma\left(1 + \frac{4}{3}\mathrm{Rd}\right)\theta' + Q\theta + \mathrm{Pr}(\theta' f - \theta f' - f' e) = 0, \tag{11}$$

$$(1 + 2\gamma\eta)\phi'' + 2\gamma\eta\phi' + \mathrm{Sc}f\phi' - k_1\mathrm{Sc}h^2\phi = 0, \tag{12}$$

$$(1 + 2\eta\gamma)h'' + \frac{\mathrm{Sc}}{\delta}fh' + 2\gamma\eta h' + k_1\frac{\mathrm{Sc}}{\delta}h^2\phi = 0. \tag{13}$$

The related boundary conditions are described as

$$\begin{aligned} &f(0) = 0, f'(0) = 1, \theta(0) = 1, \phi'(0) = k_2\phi(0), \\ &k_1 = \frac{a_0 k_c l}{W_0}, \delta h'(0) = -k_2\phi(0), \\ &f'(\infty) \to 0, \theta(\infty) \to 0, \phi(\infty) \to 0, h(\infty) \to 0. \end{aligned} \tag{14}$$

In the above equations, $\mathrm{Re} = \frac{Wz}{\nu}$ is the Reynolds number, $\gamma = \sqrt{\frac{\nu l}{W_0 R^2}}$ is the curvature factor, $\nu = \frac{\mu}{\rho}$ is the viscosity factor, $(\alpha_1, \alpha_2, \beta) = \left(\frac{\alpha_1^* W_0}{l\mu}, \frac{\alpha_2^* W_0}{l\mu}, \frac{\beta_3 W_0^2}{l^2\mu}\right)$ is the third-grade dimensionless factor, $\mathrm{Pr} = \frac{\mu C_p}{\rho}$ is the Prandtl number, $M = \frac{\sigma B_0^2 H}{\rho a}$ is the Hartman number, $\mathrm{Rd} = \frac{4\sigma^* T_\infty^3}{kk^*}$ is the radiation factor, $e = \frac{b}{a}$ is the thermal stratification factor, $k_1 = \frac{a_0 k_c l}{W_0}$ is the homogeneous reaction strength, $k_2 = \sqrt{\frac{\nu l}{W_0}}\cdot\frac{k_s}{D_A}$ is the heterogeneous reaction strength, $\delta = \frac{D_B}{D_A}$ is the quotient of diffusion coefficients, $\mathrm{Sc} = \frac{\nu}{D_A}$ is the Schmidt number, and $Q = \frac{Q_0}{\rho C_p W_w}$ is the heat generation/absorption factor.

2.1 Quantities of interest

The main quantities of engineering applications are defined mathematically as follows:

$$C_f = \frac{\tau_{rz}}{\frac{1}{2}\rho(W_z)^2} = \text{skin friction}, \quad \mathrm{Nu}_z = \frac{q_r z}{k^*(T_w - T_\infty)} = \text{Nusselt number}. \tag{15}$$

Here,

$$\tau_{rz} = 2\beta_3\left(\frac{\partial w}{\partial r}\right)^3 + \alpha_1^*\left(u\frac{\partial^2 w}{\partial r^2} + 3\frac{\partial w}{\partial r}\frac{\partial w}{\partial z} + w\frac{\partial^2 w}{\partial r \partial z} + \frac{\partial u}{\partial r}\frac{\partial w}{\partial r}\right) + 2\alpha_2^*\left(\frac{\partial u}{\partial r}\frac{\partial w}{\partial r} + \frac{\partial w}{\partial z}\frac{\partial w}{\partial r}\right) + \mu\left(\frac{\partial w}{\partial r}\right) \tag{16}$$

Making use of equation (9), we have

$$\begin{aligned} C_f(\mathrm{Re}_z)^{1/2} &= [1 + 3\alpha_1 + 2\beta_3 f''(0)]f''(0), \\ \mathrm{Nu}_z(\mathrm{Re}_z)^{-1/2} &= -\left(1 + \frac{4}{3}\mathrm{Rd}\right)\theta'(0), \end{aligned} \tag{17}$$

where $\mathrm{Re}_z = \frac{Wz}{\nu}$ is the local Reynolds number.

3 Method for the solution

The ANN approach was used to solve this problem with the addition of the Levenberg–Marquardt scheme with the backpropagation neural network algorithm (LMS-BNNA). The Levenberg–Marquardt scheme acts as a fine-tuned optimization method that improves the convergence speed of the backpropagation process. During training, the multilayer perceptron (MLP) learns by adjusting its weights to minimize a predefined cost function (usually the mean squared error [MSE]). LMS-BNNA helps in this process by iterating over the data multiple times (epochs), where each iteration improves the network's performance by reducing the error. By using LM optimization, the backpropagation algorithm is enhanced, as it reduces error faster and handles more complex datasets. The Levenberg–Marquardt method is particularly useful when the network approaches the optimal point, depending on which method leads to a quicker reduction in the error. MLP with LMS-BNNA is widely used in applications that require complex pattern recognition, such as image classification, speech recognition, and predictive analytics. It is capable of handling large amounts of data and can adapt to new information through continuous learning, making it versatile and powerful for solving real-world problems. Figure 1(b) presents the neural network process, employing an algorithmic method to optimize the design of the LMS-NNA and assess its performance using the MSE as the evaluation metric.

4 Discussion

This work investigates the influence of double stratification on a thermally radiative third-grade nanofluid flow. The fluid flowed on the stretching cylinder. It is considered that the homogeneous reaction occurs at ambient flow, while the heterogeneous reaction occurs at the wall of the cylinder. The modeled equations are converted to a dimension-free form using similarity transformations and then solved using the ANN approach. The ANN graphs and flow graphs are discussed below.

4.1 ANN graph analysis

Figure 1(b) presents the neural network process using the LMS-NNA approach. Figures 2–5 show the different scenarios for velocity, temperature, concentration, and heat transfer field against variations in different emerging factors. Figures (2–5)(a) depict the convergence of MSE for various scenarios of the modeled problem. The maximum performance of the modeled problem was obtained at epochs 295, 1,000, 687, and 117. Figures (2–5)(b) show the transitional phase of the problem for the LMS-NNA design. These visuals provide a graphical depiction of the model's progress as it moves through the various phases of solving the problem. Figures (2–5)(c) show the error histogram for the modeled problem by implementing the LMS-NNA design. An analysis of these figures shows a correlation between the evaluated error histogram (EH) values. The visual representations in Figures (2–5)(c) highlight the model's convergence and accuracy. These diagrams offer a detailed assessment of the model's precision, illustrating how closely it aligns with the expected or intended outcomes. Error histograms and convergence behavior plots provide key physical insights into a model's accuracy, stability, and efficiency. A symmetric, narrow error histogram suggests precise predictions, while skewness or a wide distribution indicates a bias or variability in the model. Outliers highlight rare but significant deviations. Convergence plots reveal how errors evolve over iterations, and smooth monotonic convergence indicates stability, oscillations suggest difficulty in optimization, and divergence points to instability or poor parameter choices. Physically, these patterns help identify model fidelity, systematic bias, noise sensitivity, and computational efficiency, thereby guiding improvements in accuracy and reliability. Figures (2–5)(d) depict the function curve fitness of the modeled problem regarding the EA structure. These graphs convey a comprehensive understanding of the optimization of the EA structure by evaluating the curve fitness using different scenarios. Figures (2–5)(e) illustrate the effectiveness of the proposed model in performing regressions across various scenarios. A review of all figures constantly reveals a pattern in which the correlation values, symbolized as "*R*," are closely assembled. This strong configuration with unity is a notable result, signifying the extraordinary exactness of the LMS-NNA design in the proposed model.

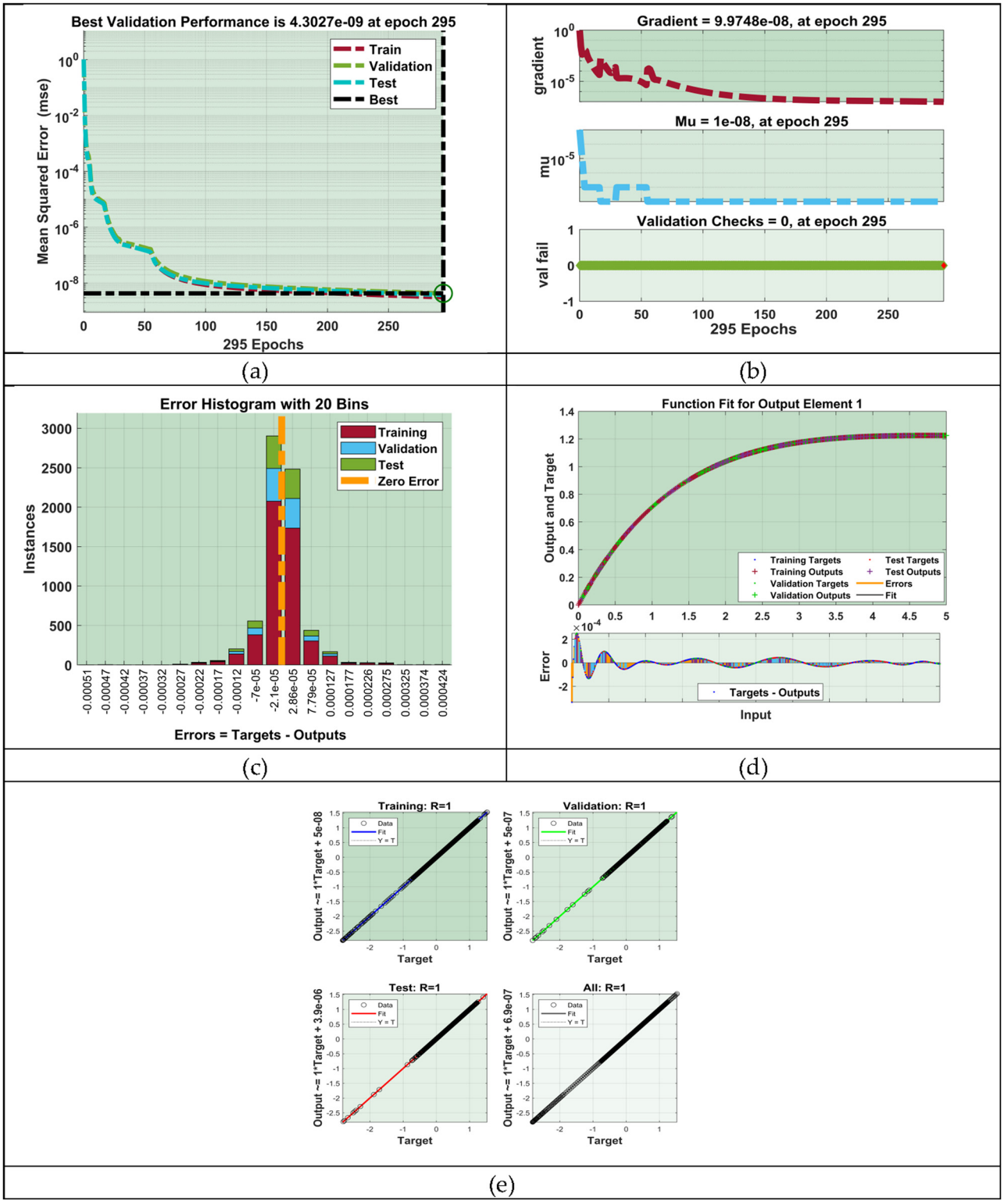

Figure 2: LMS-NNA design graphs for velocity scenario regarding (a) MSE outcomes, (b) transition state, (c) error histogram, (d) curve fitting, and (e) regression.

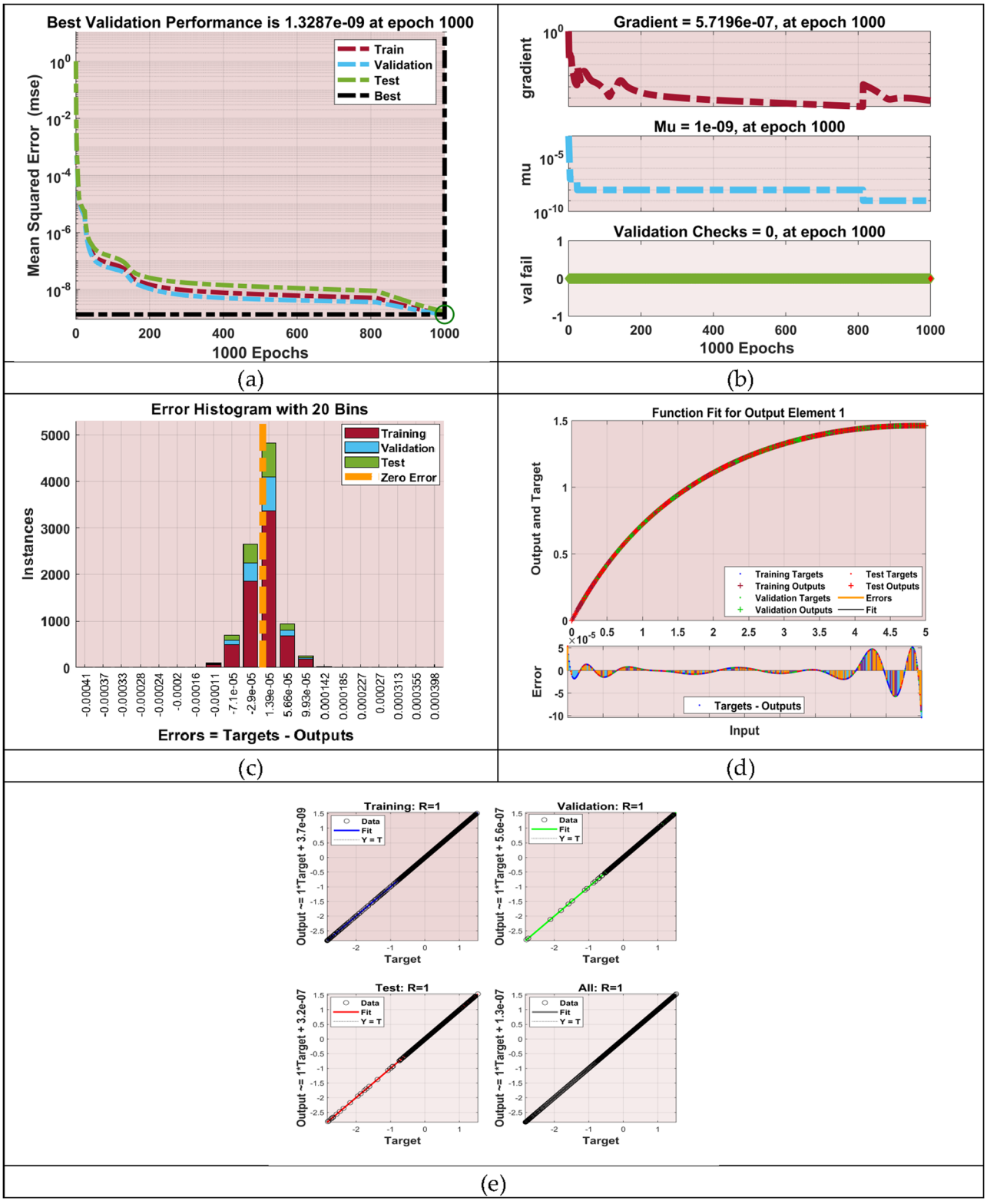

Figure 3: LMS-NNA design graphs for the temperature scenario regarding (a) MSE outcomes, (b) transition state, (c) error histogram, (d) curve fitting, and (e) regression.

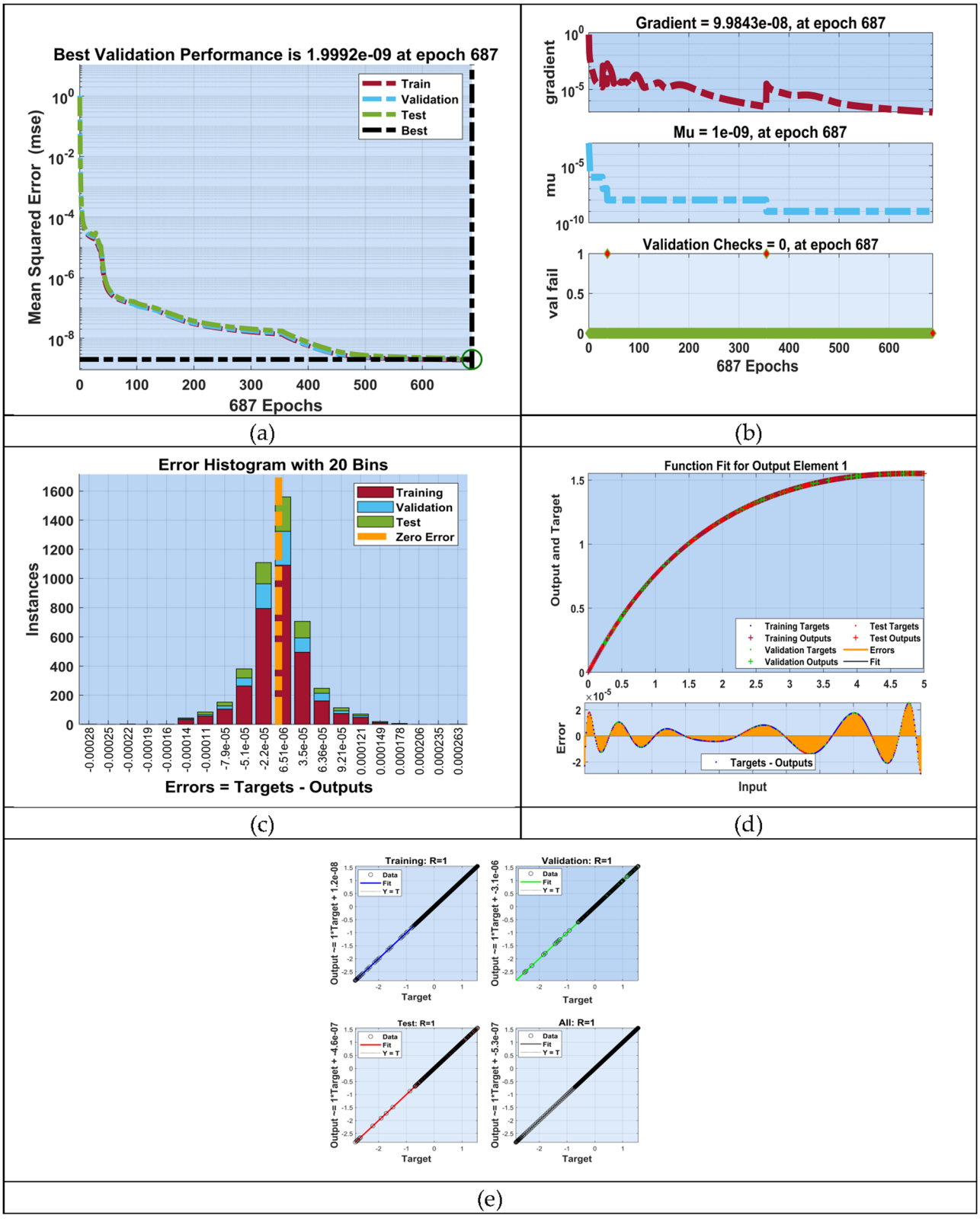

Figure 4: LMS-NNA design graphs for the concentration scenario regarding (a) MSE outcomes, (b) transition state, (c) error histogram, (d) curve fitting, and (e) regression.

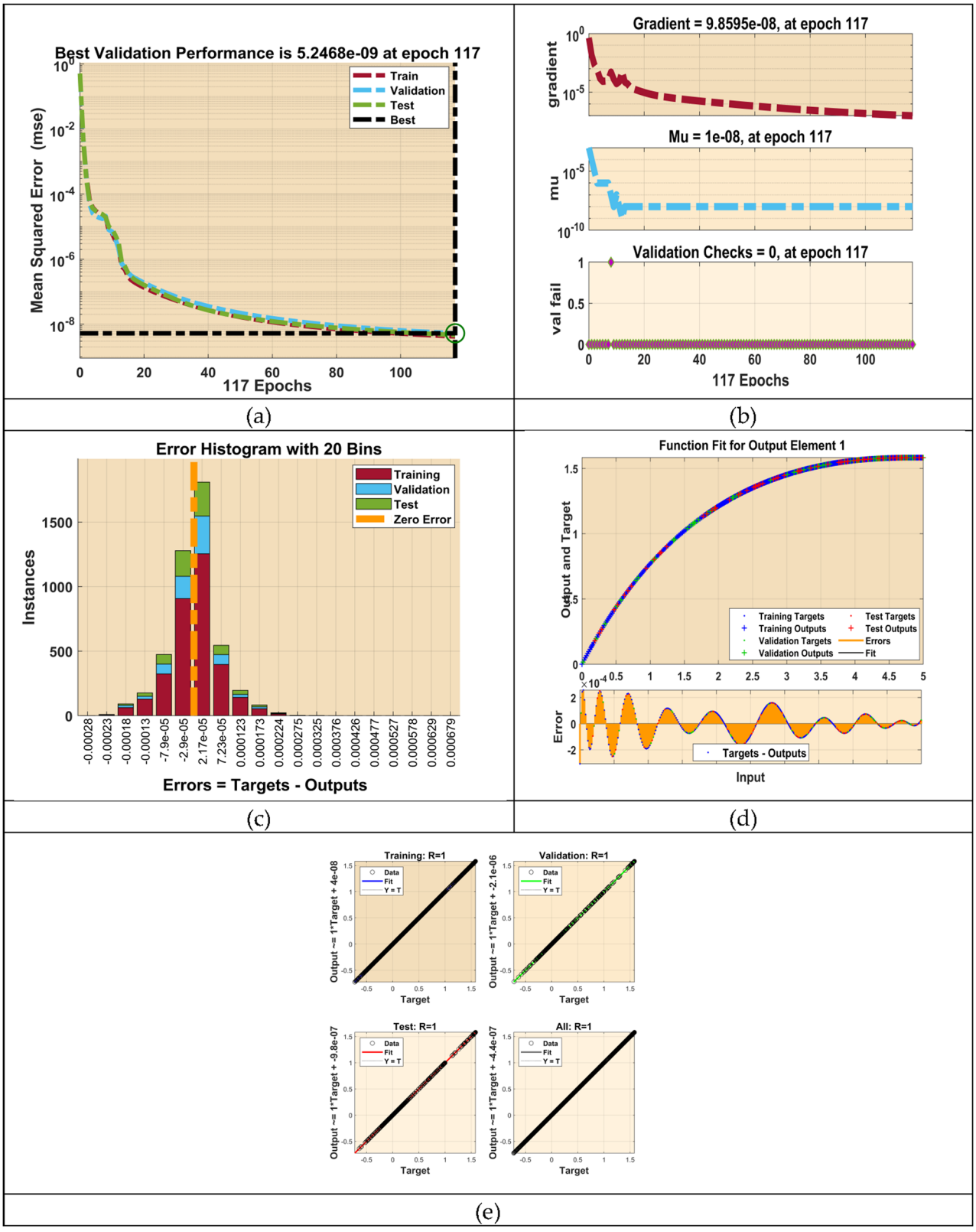

Figure 5: LMS-NNA design graphs for the heat transfer field scenario regarding (a) MSE outcomes, (b) transition state, (c) error histogram, (d) curve fitting, and (e) regression.

The sensitivity of the ANN results to variations in the network architecture, hyperparameters, and training sample size was thoroughly analyzed through detailed convergence studies for each factor:

(a) Network architecture: The effects of varying the number of layers and neurons per layer were evaluated. The findings indicate that deeper networks tend to improve performance up to a certain point, after which overfitting occurs. The convergence behavior was assessed by tracking the loss reduction over epochs.
(b) Hyperparameters: Different activation functions and learning rates were examined. The choice of activation function significantly influenced the training stability and convergence speed by considering the fastest convergence. Learning rate adjustments further highlight the trade-off between the convergence speed and stability.
(c) Number of training samples: Experiments with varying dataset sizes were conducted to understand their effect on model generalization and convergence. The investigation shows that larger training sets improve model robustness, but diminishing returns are observed beyond the threshold.

4.2 Velocity characteristics

The impacts of various factors on the velocity distribution $f'(\eta)$ are shown in Figure 6(a)–(f). Figure 6(a) portrays the effects of the third-grade dimensionless factor α_2. With the progression in α_2, there is a corresponding augmentation in $f'(\eta)$. As this factor increases, it suggests that the influence of non-linear material properties becomes more noticeable. A corresponding augmentation in the velocity distribution $f'(\eta)$ indicates that the fluid flow is increasingly influenced by these non-linear effects. Physically, this means that the fluid experiences enhanced shear-thinning or shear-thickening behaviors, where the region of the cylindrical surface with higher velocity gradients changes its flow properties due to the material's internal structure. The augmentation in $f'(\eta)$ also implies that the flow becomes more sensitive to boundary conditions and external forces. Figure 6(b) shows the absolute error (AE) for variations in α_2 against $f'(\eta)$ using the LMS-NNA design for the modeled problem. For the current problem, these errors vary within the range of 10^{-3} –10^{-7}, as depicted in Figure 6(b). The AE in the current study focuses on the differences in computation between predicted and actual results, offering insights into how accurately the current model addresses the problem at hand. Moreover, by analyzing the numerical AE results alongside the reference outputs, it is evident that the developed ANN models exhibit a notable level of accuracy, thereby validating their effectiveness and dependability. Figure 6(c) depicts the impacts of the curvature factor of the cylinder γ. For fluid flow on a stretching cylinder, an increase in the curvature factor γ (*i.e.*, reduction in the cylinder's radius) leads to a reduction in the velocity distribution. Physically, this occurs because as the cylinder stretches while becoming more curved, the fluid particles experience greater resistance to maintaining high velocities. The stretching effect tends to draw fluid along the surface, but the increased curvature forces the fluid to follow a more tightly curved path, increasing the centrifugal forces and boundary layer thickness. This increased curvature reduces the fluid's ability to adhere closely to the surface, leading to a reduction in the velocity distribution. The stretching and curvature effects create more resistance to fluid acceleration, slowing down the overall flow near the cylinder's surface, as shown in Figure 6(c). Figure 6(d) depicts the AE for variations in γ against $f'(\eta)$ using the LMS-NNA design for the modeled problem. For the current problem, these errors vary within the range of 10^{-4}–10^{-7}, as depicted in Figure 6(d). The AE in the current study focuses on the differences in computation between predicted and actual results, offering insights into how accurately the current model addresses the problem at hand. Figure 6(e) depicts the impact of the magnetic factor M on $f'(\eta)$. The growth in the magnetic field M leads to an increased magnetic field strength around the stretching cylinder that exerts a Lorentz force on the fluid around the cylinder. This force acts to dampen the motion of the fluid particles, resulting in a reduction in their velocity distribution $f'(\eta)$ as they flow along the surface of the cylinder. Physically, this means that the stronger the magnetic field, the more it resists the fluid's natural tendency to flow freely, leading to a more uniform and slower velocity profile. Consequently, as the magnetic factor increases, the energy imparted to the fluid from the stretching cylinder is countered by the magnetic drag, resulting in lower fluid velocities and altered flow characteristics, as depicted in Figure 6(e). Figure 6(f) depicts the AE for variations in M against $f'(\eta)$ using the LMS-NNA design for the modeled problem. For the current problem, these errors vary within the range 10^{-3}–10^{-7}, as depicted in Figure 6(f).

4.3 Temperature characteristics

The influences of variations in various emerging factors on the thermal distribution $\theta(\eta)$ are shown in Figure 7(a)–(j). The impression of the curvature factor γ on $\theta(\eta)$ is illustrated in Figure 7(a). As γ increases for the fluid flow on a stretching cylinder, it enhances the thermal distribution

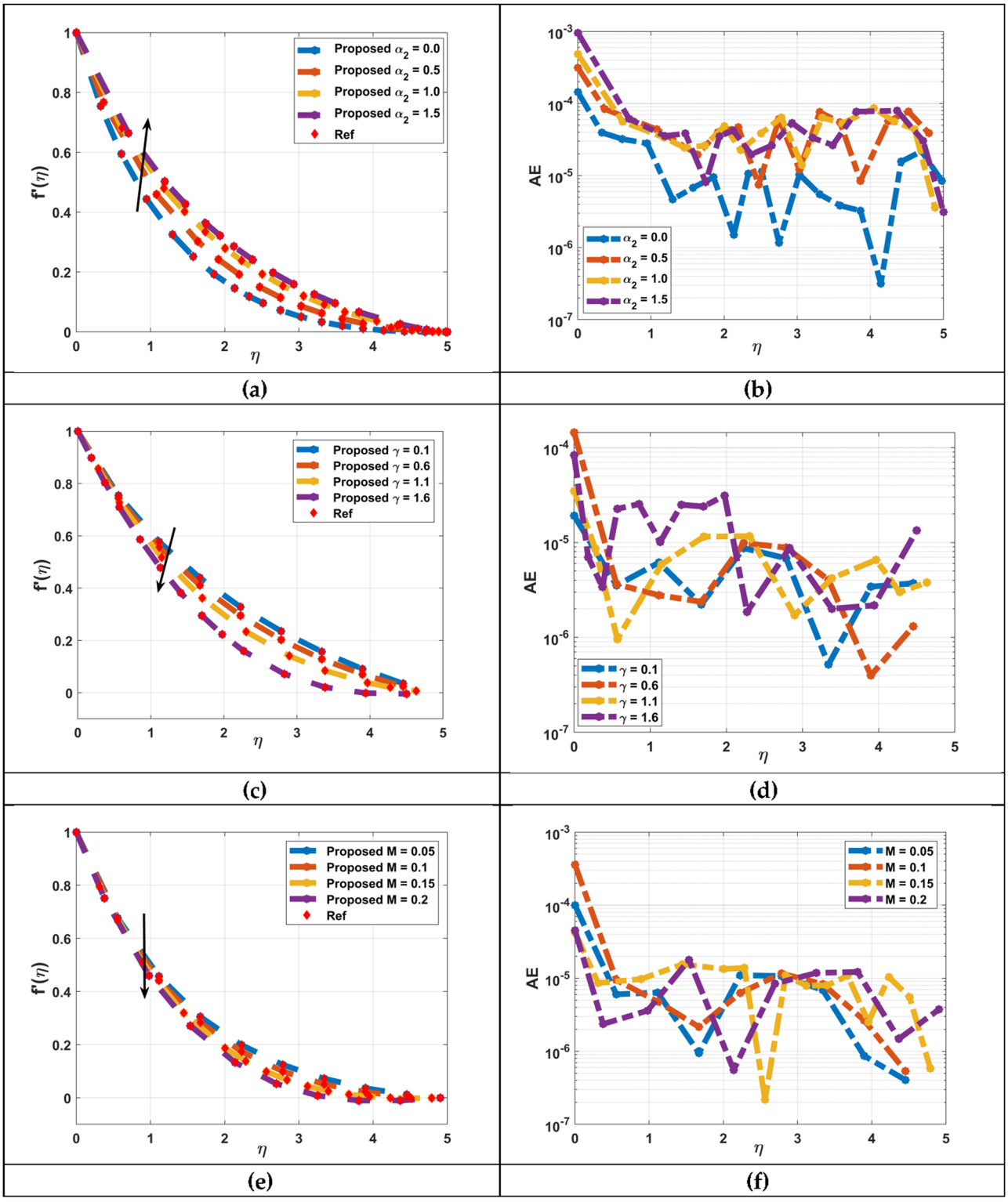

Figure 6: (a) Impact of α_2 on $f'(\eta)$, (b) AE for variations in α_2, (c) impact of γ on $f'(\eta)$, (d) AE for variations in γ, (e) impact of M on $f'(\eta)$, and (f) AE for variations in M.

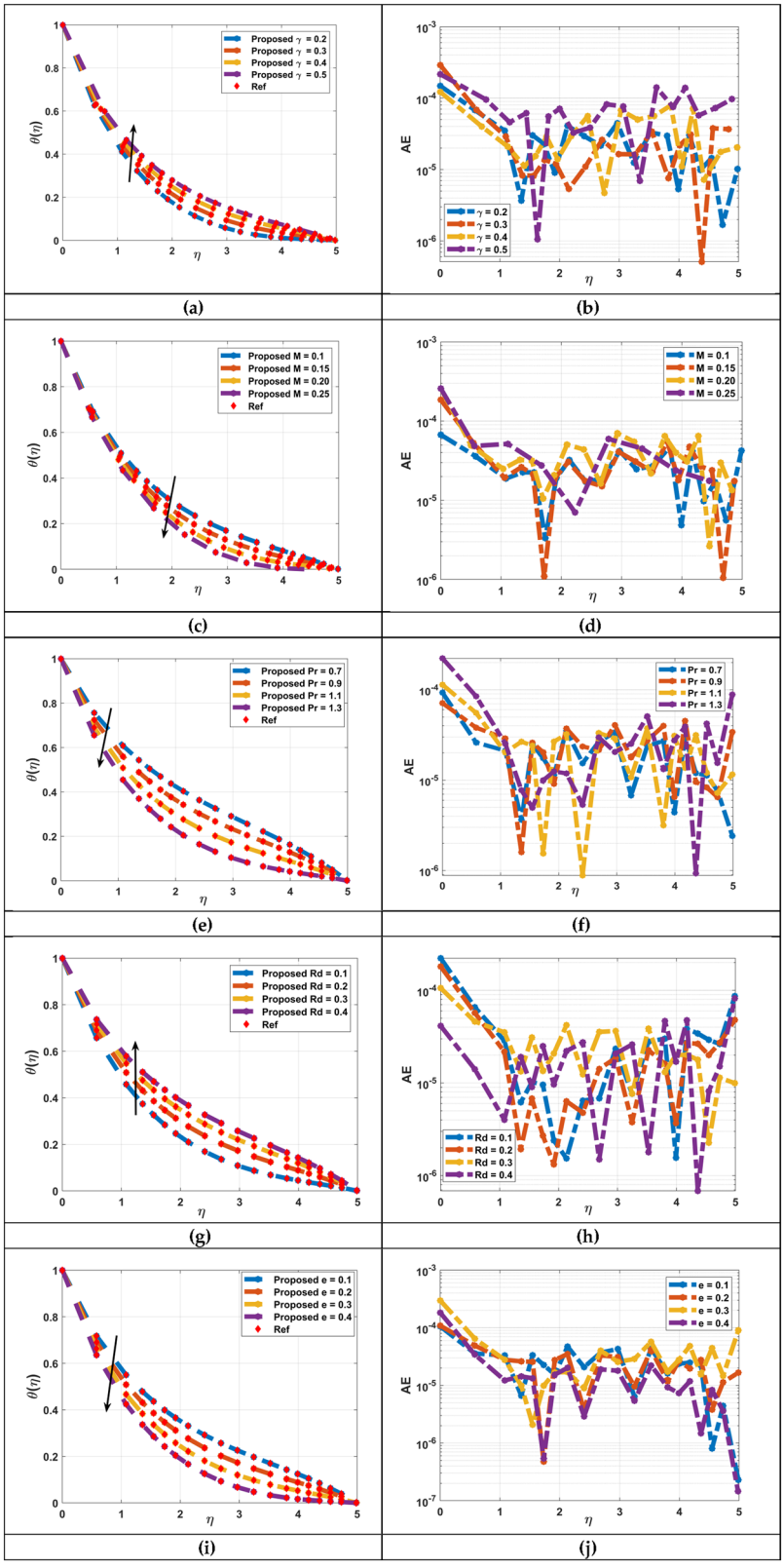

Figure 7: (a) Impact of γ on $\theta(\eta)$, (b) AE for variations in γ, (c) impact of M on $\theta(\eta)$, (d) AE for variations in M, (e) impact of Pr on $\theta(\eta)$, (f) AE for variations in Pr, (g) impact of Rd on $\theta(\eta)$, (h) AE for variations in Rd, (i) impact of e on $\theta(\eta)$, and (j) AE for variations in e.

$\theta(\eta)$ within the fluid. This is primarily because the curvature creates a more complex flow pattern, which increases the surface area available for heat transfer between the cylinder and fluid. The tighter the curvature, the more the fluid particles are forced to interact with the heated surface, leading to improved heat conduction and convection processes. As a result, the thermal energy is more effectively distributed throughout the fluid, promoting a higher temperature gradient and enhancing the overall thermal efficiency. Physically, this means that the fluid absorbs heat more rapidly and uniformly, which influences properties like viscosity and thermal conductivity, ultimately affecting the flow behavior around the cylinder. Figure 7(b) depicts the AE for variations in γ against $\theta(\eta)$ using the LMS-NNA design for the modeled problem. For the current problem, these errors vary within the range of 10^{-3}–10^{-6}, as depicted in Figure 7(b). The influence of the magnetic factor M on $\theta(\eta)$ is depicted in Figure 7(c). As M increases in the fluid flow on the stretching cylinder, the thermal distribution $\theta(\eta)$ tends to diminish due to the effect of the magnetic field on the flow dynamics. A higher M leads to a stronger Lorentz force acting on the electrically conductive fluid. This force not only dampens the fluid motion but also alters the flow patterns, resulting in reduced convective heat transfer efficiency. The magnetic field restricts the fluid's natural mixing, which is essential for even heat distribution, causing thermal energy to become concentrated on the surface of the cylinder rather than being uniformly dispersed. Consequently, the overall temperature gradient within the fluid becomes less effective, leading to a reduction in $\theta(\eta)$, as the magnetic influence inhibits the fluid's ability to uniformly transport and distribute heat along the stretching cylinder. Figure 7(d) depicts the AE for variations in M against $\theta(\eta)$ using the LMS-NNA design for the modeled problem. For the current problem, these errors vary within the range of 10^{-3}–10^{-6}, as depicted in Figure 7(d). By analyzing the numerical AE results alongside the reference outputs, it is evident that the developed ANN models exhibit a notable level of accuracy, thereby validating their effectiveness and dependability. The impression of the Prandtl number Pr on $\theta(\eta)$ is illustrated in Figure 7(e). As Pr increases for the fluid flow on the stretching cylinder, there is a reduction in $\theta(\eta)$ due to the relative effects of momentum and thermal diffusivities. A higher Pr indicates that momentum diffuses more rapidly than heat, leading to a thicker thermal layer at the boundary compared to the velocity layer at the boundary, as observed by Akbar *et al.* [45]. This means that while the fluid is able to maintain its momentum, it is less effective at conducting heat away from the cylinder surface. As a result, the thermal energy from the cylinder does not distribute evenly throughout the fluid, leading to localized heating and a less uniform temperature profile. The diminished interaction between the fluid layers further reduces the overall thermal distribution, which delays the efficiency of the heat transfer processes in the flow, as shown in Figure 7(e). Figure 7(f) illustrates the AE for variations in Pr against $\theta(\eta)$ using the LMS-NNA design for the modeled problem. For the current problem, these errors vary within the range of 10^{-3}–10^{-6}, as depicted in Figure 7(f). An examination of the numerical AE results, in conjunction with the reference outputs, demonstrated that the developed ANN models showed a significant degree of accuracy, confirming their reliability and effectiveness. Figure 7(g) shows the impact of the radiation parameter Rd on $\theta(\eta)$. As Rd increases for the fluid flowing on a stretching cylinder, the thermal distribution $\theta(\eta)$ improves due to the enhanced transfer of heat through radiation in addition to conduction and convection. A higher Rd signifies that the thermal radiation emitted by the cylinder surface is more significant. This radiative heat transfer allows for a more effective energy exchange between the cylinder and surrounding fluid, promoting a more uniform temperature distribution $\theta(\eta)$. As a result, the fluid absorbs thermal energy more efficiently, leading to a more even spread of temperature throughout the flow. This augmentation in the thermal distribution $\theta(\eta)$ enhances the overall thermal performance, optimizing the heat transfer processes around the stretching cylinder, as depicted in Figure 7(g). Figure 7(h) depicts the AE for variations in Rd against $\theta(\eta)$ using the LMS-NNA design for the modeled problem. For the current problem, these errors vary within the range of 10^{-3}–10^{-6}, as depicted in Figure 7(h). Figure 7(i) depicts the impact of the thermal stratification factor e on $\theta(\eta)$. As the thermal stratification factor e increases, it indicates a greater degree of layering or separation of the temperatures within the fluid surrounding the stretching cylinder. This enhanced stratification leads to a reduced thermal distribution $\theta(\eta)$, meaning that the heat from the cylinder is less effectively transferred to the fluid. In essence, the fluid layers become more distinct, with cooler layers failing to mix adequately with warmer ones, resulting in a decreased ability to equilibrate temperature differences. This effect delays the cooling or heating efficiency of the cylinder, impacting processes like heat exchange and influencing the overall thermal behavior of the system. Hence, an increase in e results in a reduction in $\theta(\eta)$, as shown in Figure 7(i). Figure 7(h) depicts the AE for variations in Rd against $\theta(\eta)$ using the LMS-NNA design for the modeled problem. For the current problem, these errors vary within the range of 10^{-3}–10^{-6}, as depicted in Figure 7(h).

4.4 Concentration characteristics

The impact of various factors on the concentration distribution $\phi(\eta)$ is shown in Figure 8(a)–(g). The impacts of the curvature factor γ on $\phi(\eta)$ are shown in Figure 8(a). The increase in γ for the fluid flow on a stretching cylinder indicates that as the curvature of the cylinder increases, the surface area exposed to the fluid flow becomes larger. This leads to an augmentation in the concentration distribution, as more fluid particles interact with the surface of the cylinder. Physically, this can be understood as a stronger influence of the cylinder geometry on the fluid behavior. The stretching motion of the cylinder enhances diffusion and transport phenomena, which results in a more prominent distribution of concentration near the surface of the cylinder, as depicted in Figure 8(a). Figure 8(b) depicts the AE for variations in γ against $\phi(\eta)$ using the LMS-NNA design for the modeled problem. For the current problem, these errors vary within the range of 10^{-4}–10^{-6}, as depicted in Figure 8(b). The impact of the Schmidt number Sc on $\phi(\eta)$ is shown in Figure 8(c). When Sc increases for fluid flow on the stretching cylinder, momentum diffusion (or viscous effects) prevails more than mass diffusion. Physically, this means that the solute in the fluid takes longer to diffuse or spread out across the flow on the surface of the cylinder. As a result, the concentration layer at the boundary becomes thinner, leading to a steeper concentration gradient near the cylinder's surface. This augmentation in concentration distribution is because the slower diffusion of mass keeps the solute more concentrated near the surface of the cylinder, enhancing the localized concentration in the boundary layer region. Figure 8(d) illustrates the AE for variations in Sc against $\phi(\eta)$ using the LMS-NNA design for the modeled problem. For the current problem, these errors vary within the range of 10^{-4}–10^{-8}, as depicted in Figure 8(d). The impact of the quotient of the diffusion coefficients δ on $\phi(\eta)$ is shown in Figure 8(e). For fluid flow on a stretching cylinder, an increase in δ typically means that the fluid has heat that spreads more quickly within the boundary layer. As a result, the concentration distribution of the solute becomes more dispersed. This occurs because the higher diffusivity ratio allows the particles to spread more efficiently throughout the fluid, reducing sharp concentration gradients and leading to smoother and more uniform distributions. Physically, this can be seen as an enhancement of the mixing and diffusion processes, promoting a more even distribution of the fluid properties across the flow field. Ultimately, growth in the diffusion coefficient quotient δ results in augmentation of the concentration distribution $\phi(\eta)$. Figure 8(f) depicts the AE for variations in δ against $\phi(\eta)$ using the LMS-NNA design for the modeled problem. For the current problem, these errors vary within the range of 10^{-4}–10^{-8}, as depicted in Figure 8(f). The impact of the homogeneous reaction strength factor k_1 on $\phi(\eta)$ is shown in Figure 8(g). The reduction in the concentration distribution $\phi(\eta)$ with an increase of the homogeneous reaction strength factor for a fluid flow on a stretching cylinder can be understood as follows: in the case of a homogeneous reaction, the reactants are uniformly distributed within the fluid, and as the reaction progresses, reactants are consumed. A higher reaction strength means that the reaction rate is faster, which leads to a quicker depletion of the reactant concentration near the surface of the cylinder. This causes a sharper concentration gradient, particularly near the cylinder surface, where the stretching motion promotes fluid flow. Consequently, as the strength of the reaction increases, the concentration of the reactants reduces more rapidly, leading to a lower overall distribution of concentration in the flow field near the surface of the cylinder. Figure 8(h) depicts the AE for variations in k_1 against $\phi(\eta)$ using the LMS-NNA design for the modeled problem. For the current problem, these errors vary within the range of 10^{-4}–10^{-8}, as depicted in Figure 8(h). The impact of the heterogeneous reaction strength factor k_2 on $\phi(\eta)$ is shown in Figure 8(i). The increase in the heterogeneous reaction strength factor indicates that the chemical reactions occurring at the surface of the stretching cylinder become more intense. This leads to a faster conversion of reactants into products at the surface of the cylinder. As a result, the concentration of the reactant near the surface decreases more rapidly because it is consumed more quickly by the reaction. This reduction in reactant concentration creates a steeper concentration gradient, leading to more efficient transport of reactants from the bulk fluid toward the cylinder surface. Consequently, the concentration distribution $\phi(\eta)$ within the fluid flow decreases as the reaction strength increases, especially near the surface of the cylinder where the reaction is strongest, as depicted in Figure 8(i). Figure 8(j) depicts the AE for variations in k_2 against $\phi(\eta)$ using the LMS-NNA design for the modeled problem. For the current problem, these errors vary within the range of 10^{-4}–10^{-8}, as depicted in Figure 8(j).

4.5 Heat transfer field

The impact of various emerging factors on the heat transfer field $h(\eta)$ is depicted in Figure 9(a)–(h). The influence of the quotient of the diffusion coefficients δ on $h(\eta)$ is depicted in Figure 9(a). The reduction in the heat transfer

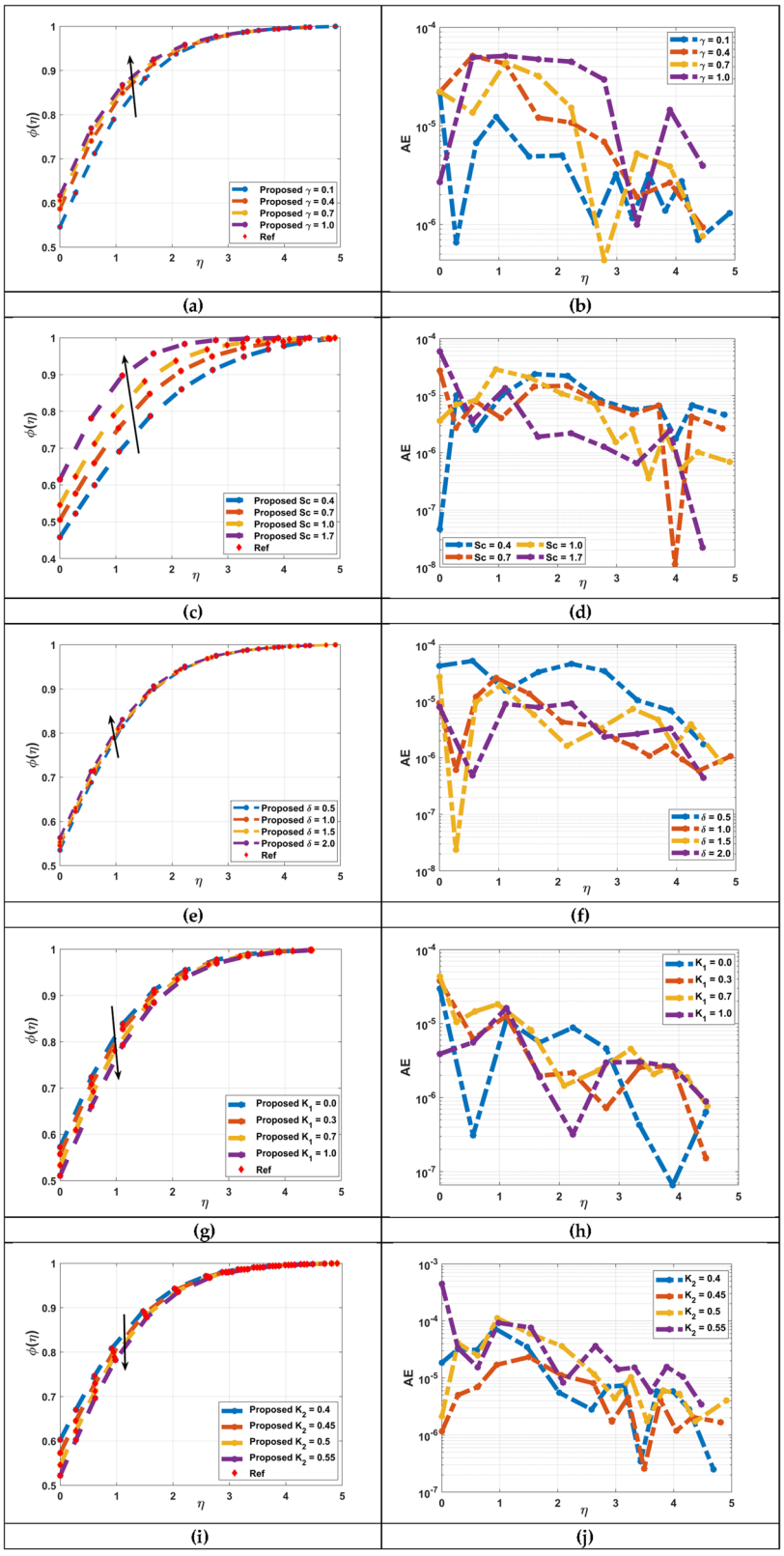

Figure 8: (a) Impact of γ on $\phi(\eta)$, (b) AE for variations in γ, (c) impact of Sc on $\phi(\eta)$, (d) AE for variations in Sc, (e) impact of δ on $\phi(\eta)$, (f) AE for variations in δ, (g) impact of k_1 on $\phi(\eta)$, (h) AE for variations in k_1, (i) impact of k_2 on $\phi(\eta)$, and (j) AE for variations in k_2.

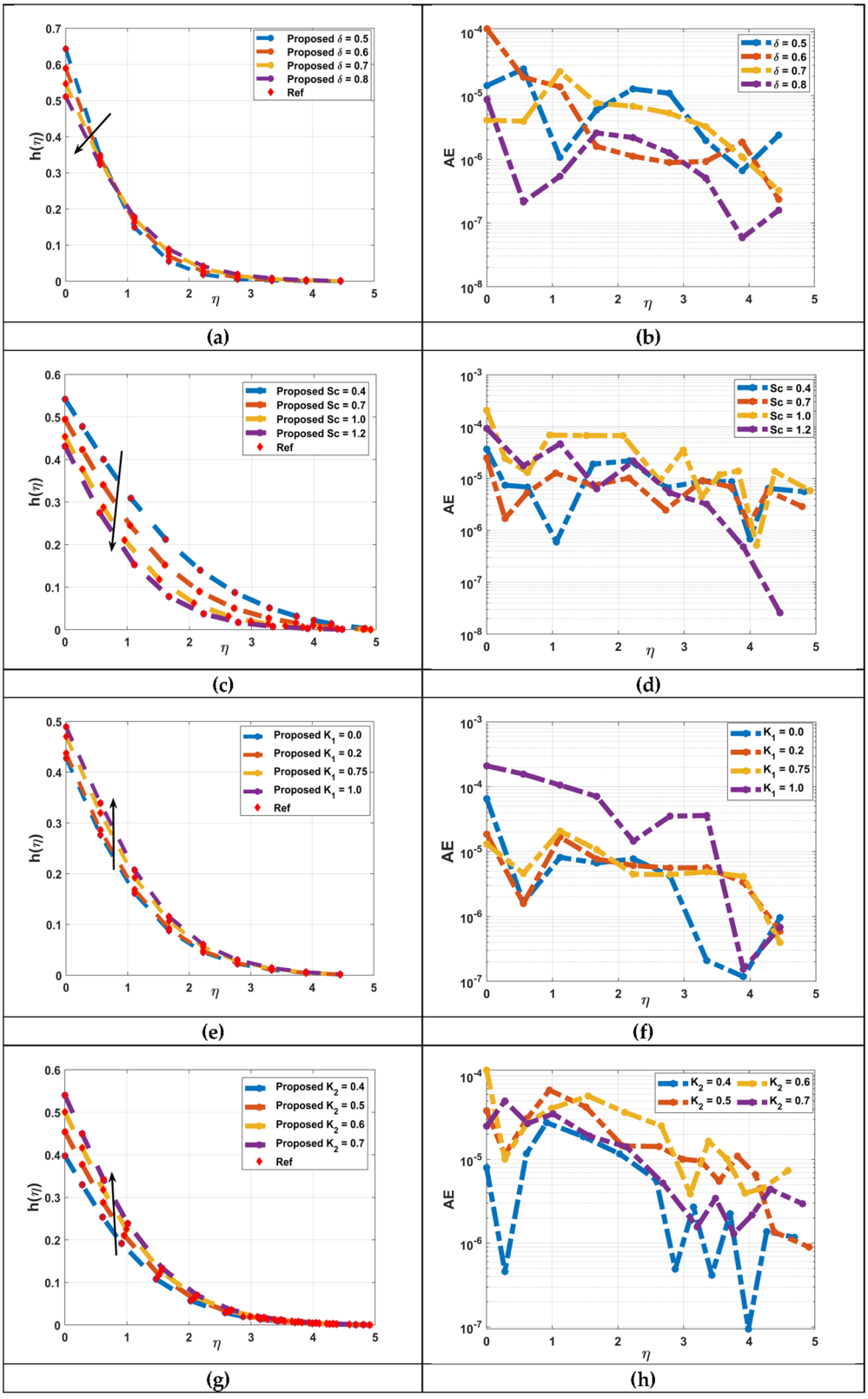

Figure 9: (a) Impact of δ on $h(\eta)$, (b) AE for variations in δ, (c) impact of Sc on $h(\eta)$, (d) AE for variations in Sc, (e) impact of k_1 on $h(\eta)$, (f) AE for variations in k_1, (g) impact of k_2 on $h(\eta)$, and (h) AE for variations in k_2.

field with an increase in δ for fluid flow on the stretching cylinder can be physically interpreted as the quotient of the diffusion coefficients, which typically involves the ratio of thermal diffusivity to mass diffusivity and plays a crucial role in energy transfer. As this ratio increases, thermal diffusion dominates, meaning that heat spreads more quickly throughout the fluid than mass diffusion. This rapid spreading reduces the temperature gradient near the surface of the cylinder, leading to a lower rate of heat transfer to or from the cylinder. Essentially, the fluid's ability to transfer heat diminishes as the thermal diffusion outpaces the other forms of diffusion, causing a reduction in the overall heat transfer field, as portrayed in Figure 9(a). Figure 9(b) depicts the AE for variations in δ against $h(\eta)$ using the LMS-NNA design for the modeled problem. For the current problem, these errors vary within the range of 10^{-4}–10^{-7}, as depicted in Figure 9(b). The influence of the quotient of the diffusion coefficients Sc on $h(\eta)$ is depicted in Figure 9(c). As the Schmidt number Sc increases for the fluid flow on the stretching cylinder, there is a reduction in the heat transfer field. By definition, a higher Sc indicates that mass diffusion is slower than momentum diffusion. In this context, the lower rate of mass diffusion results in a thinner concentration layer at the boundary around the cylinder, reducing the mixing of heat with the surrounding fluid. Since heat transfer relies on the flow and diffusion of fluid particles, the decreased mixing due to high Sc leads to a weaker temperature gradient and thus a reduction in the heat transfer field. Essentially, with limited mass transport, heat cannot diffuse as efficiently, lowering the heat transfer rate on the surface of the cylinder, as depicted in Figure 9(c). Figure 9(d) depicts the AE for variations in Sc against $h(\eta)$ using the LMS-NNA design for the modeled problem. For the current problem, these errors vary within the range of 10^{-4}–10^{-8}, as depicted in Figure 9(d). The influence of the homogeneous reaction strength factor k_1 on $h(\eta)$ is shown in Figure 9(e). An increase in k_1 for the fluid flow on the stretching cylinder leads to an augmentation in the heat transfer field. Actually, k_1 represents the intensity of a chemical reaction occurring uniformly within the fluid. As the reaction strength increased, more heat was generated within the fluid owing to the exothermic nature of the reaction. This internal heat production enhances the local thermal energy, increasing the temperature gradient between the fluid and the cylinder surface. A stronger temperature gradient facilitates greater heat transfer from the fluid to the cylinder, and *vice versa*. Thus, the enhanced reaction increases the heat transfer field by introducing additional thermal energy through the reaction process, boosting the overall rate of heat exchange. Hence, with an increase in k_1, there is corresponding augmentation in $h(\eta)$, as shown in Figure 9(e). Figure 9(f) depicts the AE for variations in k_1 against $h(\eta)$ using the LMS-NNA design for the modeled problem. For the current problem, these errors vary within the range of 10^{-4}–10^{-7}, as depicted in Figure 9(f). The influence of the heterogeneous reaction strength factor k_2 on $h(\eta)$ is shown in Figure 9(g). From this graphical view, it has noticed that, as k_2 increases for the fluid flow on the stretching cylinder, there is an augmentation in the heat transfer field. Actually, a heterogeneous reaction occurs at the interface between the surface of the cylinder and the fluid, unlike a homogeneous reaction that occurs uniformly in the bulk of the fluid. When the strength of this surface-based reaction increases, more heat is generated directly at the boundary layer between the fluid and cylinder. This localized heat production enhances the temperature difference between the cylinder surface and the surrounding fluid, thereby increasing the thermal gradient. Thus, the increase in heterogeneous reaction strength boosts heat transfer by intensifying the thermal interactions at the surface–fluid interface, as shown in Figure 9(g). Figure 9(h) depicts the AE for variations in k_2 against $h(\eta)$ using the LMS-NNA design for the modeled problem. For the current problem, these errors vary within the range of 10^{-4}–10^{-7}, as depicted in Figure 9(h).

4.6 Asymptotic behavior of flow profiles

The asymptotic behavior of the velocity, temperature, and concentration profiles under extreme values of the governing parameters provides crucial insights into the

Table 1: LMS-NNA design results for various scenarios

Scenarios	MSE			Performance	Gradient	Mu	Epoch	Time (s)
	Training	Validation	Testing					
1	3.1152×10^{-9}	4.4325×10^{-9}	3.4325×10^{-9}	3.12×10^{-9}	9.97×10^{-8}	1.00×10^{-8}	295	01
2	1.3652×10^{-9}	1.3455×10^{-9}	1.6744×10^{-9}	1.36×10^{-9}	5.72×10^{-7}	1.00×10^{-9}	1,000	08
3	1.8991×10^{-9}	1.9994×10^{-9}	2.4321×10^{-9}	1.90×10^{-9}	9.98×10^{-8}	1.00×10^{-8}	687	03
4	4.5432×10^{-9}	5.4352×10^{-9}	4.4352×10^{-9}	4.22×10^{-9}	9.86×10^{-8}	1.00×10^{-8}	117	01

Table 2: Cooperative results for $\theta'(0)$ considering variations in Pr

Pr	Ali *et al.* [43] results	Kumari and Nath [44] results	Current results
0.7	0.4552	0.4560	0.45451
2.0	0.9108	0.9117	0.91091
7.0	1.8944	1.8977	1.89521

physical characteristics of the flow. At high Reynolds numbers, inertial forces dominate the viscous forces, resulting in thinner boundary layers with steep velocity, temperature, and concentration gradients near the surface. Under a strong magnetic field (high Hartmann number), Lorentz forces suppress turbulence, leading to a nearly stagnant core flow, weaker convective heat transfer, and more uniform temperature and concentration distributions. In strongly stratified flows, buoyancy forces influence the velocity depending on the temperature gradient, causing either suppression or enhancement of flow, while temperature and concentration profiles exhibit significant layering or mixing based on the stratification conditions.

4.7 Table discussion

Table 1 provides information about MSE comprising testing, training, and validation. This table also shows the performance, mu parameter, and gradient of the molded problem with the implementation of the LMS-NNA design. It can be observed from this table that the optimal performance of the model is achieved at epochs 275, 1,000, 687, and 117 in all four scenarios of the modeled problem. The data shown at these specific epochs represent moments during training when these metrics were assessed. The variations observed across epochs provide important insights into how the network learns, converges, and adjusts its parameters for better performance. This information helps refine the model and enables the selection of optimal parameters suited to the given ANN architecture. To ensure the validation of the current investigations, a detailed comparative analysis was conducted by systematically matching the obtained results with the well-established findings of Ali *et al.* [43] and Kumari and Nath [44]. This comparison was performed by specifically analyzing the variations in the Prandtl number while deliberately neglecting all other emerging influencing factors to maintain consistency in the assessment. The results of this comparative analysis are presented in Table 2, which clearly highlights a strong correlation between the present findings and the previously reported results. The close agreement observed across all datasets confirms the accuracy and reliability of the current investigation, reinforcing its validity and credibility within the scientific domain.

5 Conclusions

This work investigates the influences of double stratification on a thermally radiative third-grade nanofluid flow. The fluid flows on a stretching cylinder. It is considered that the homogeneous reaction occurs at an ambient flow, while the heterogeneous reaction occurs at the wall of the cylinder. The modeled equations are converted to dimension-free form using similarity transformations and then solved by using the ANN approach. The impacts of various factors on different flow profiles have been discussed comprehensively. After an in-depth study of the work, it was observed that:

- The maximum performance of the modeled problem was obtained at epochs 295, 1,000, 687, and 117 using the LMS-NNA design.
- The error histogram (EH) for the modeled problem revealed a correlation between the evaluated EH values by using the LMS-NNA design that highlights the model's convergence and accuracy.
- The velocity characteristics of the fluid decreased with an increase in the magnetic and curvature factors and increased with an increase in the third-grade dimensionless factor.
- The temperature distribution diminished with an increase in the curvature factor of the cylinder, magnetic factor, Prandtl number, and thermal stratification factor, while it increased with an increase in the radiation factor.
- The concentration profiles increased with an increase in the curvature factor of the cylinder; the Schmidt number and quotient of the diffusion coefficients decreased with an increase in the homogeneous/heterogeneous reaction strength factors.
- The heat transfer field decreased with an increase in the Schmidt number and quotient of the diffusion coefficients, whereas it increased with an increase in the homogeneous/heterogeneous reaction strength factors.
- For all four scenarios, the gradient values are associated at 9.97×10^{-8}, 5.72×10^{-7}, 9.98×10^{-8}, and 9.86×10^{-8} with the corresponding epochs 295, 1,000, 687, and 117.
- The AE values were evaluated for all the four scenarios that fall within the range of 10^{-3}–10^{-8} and associated with the corresponding ANN configuration that demonstrates a fine degree of accuracy.

Funding information: This work was supported by the Deanship of Scientific Research, the Vice Presidency for

Graduate Studies and Scientific Research, King Faisal University Saudi Arabia (Grant No. KFU252420). This study was supported *via* funding from Prince Sattam bin Abdulaziz University project number (PSAU/2025/R/1446).

Author contributions: All authors have accepted responsibility for the entire content of this manuscript and approved its submission.

Conflict of interest: The authors state no conflict of interest.

Data availability statement: All data generated or analyzed during this study are included in this published article.

References

[1] Reddy YD, Goud BS, Nisar KS, Alshahrani B, Mahmoud M, Park C. Heat absorption/generation effect on MHD heat transfer fluid flow along a stretching cylinder with a porous medium. Alexandria Eng J. 2023;64:659–66.

[2] Lone SA, Khan A, Raiza Z, Alrabaiah H, Shahab S, Saeed A, et al. A semi-analytical solution of the magnetohydrodynamic blood-based ternary hybrid nanofluid flow over a convectively heated bidirectional stretching surface under velocity slip conditions. AIP Adv. 2024;14(4):1–13.

[3] Smolentsev S. Physical background, computations and practical issues of the magnetohydrodynamic pressure drop in a fusion liquid metal blanket. Fluids. 2021;6(3):110.

[4] Lao LL, Liu YQ, Turnbull AD. Magnetic-confinement fusion—plasma theory: Tokamak magnetohydrodynamic equilibrium and stability. San Diego, CA (United States): General Atomics; 2021.

[5] Ahmad B, Ahmad MO, Farman M, Akgül A, Riaz MB. A significance of multi slip condition for inclined MHD nano-fluid flow with non linear thermal radiations, Dufuor and Sorrot, and chemically reactive bio-convection effect. S Afr J Chem Eng. 2023;43:135–45.

[6] Tarakaramu N, Satya Narayana PV, Sivakumar N, Harish Babu D, Bhagya Lakshmi K. Convective conditions on 3D magnetohydrodynamic (MHD) non-Newtonian nanofluid flow with nonlinear thermal radiation and heat absorption: a numerical analysis. J Nanofluids. 2023;12(2):448–57.

[7] Rafique K, Mahmood Z, Khan U. Mathematical analysis of MHD hybrid nanofluid flow with variable viscosity and slip conditions over a stretching surface. Mater Today Commun. 2023;36:106692.

[8] Thabet EN, Khan Z, Abd-Alla AM, Bayones FS. Thermal enhancement, thermophoretic diffusion, and Brownian motion impacts on MHD micropolar nanofluid over an inclined surface: numerical simulation. Numer Heat Transf, Part A. 2023;28:1–20.

[9] Choi SU, Eastman JA. Enhancing thermal conductivity of fluids with nanoparticles (No. ANL/MSD/CP-84938; CONF-951135-29). IL (United States): Argonne National Lab.; 1995.

[10] AL-Essa LA, Almutlak SA, Lone SA, Raizah Z, Saeed A, Khan A. Investigation of the flow behavior of a water-based hybrid nanofluid containing silver and titanium oxide nanomaterials between two angular rotating disks: A numerical approach. Mod Phys Lett B. 2024;39:2450486.

[11] Akbar NS, Zamir T, Noor T, Muhammad T, Ali MR. Heat transfer enhancement using ternary hybrid nanofluid for cross-viscosity model with intelligent Levenberg-Marquardt neural networks approach incorporating entropy generation. Case Stud Therm Eng. 2024;63:105290.

[12] Shah FA, Akbar NS, Zamir T, Abd El-Rahman M, Khan WA. Thermal energy analysis using artificial neural network and particle swarm optimization approach in partially ionized hyperbolic tangent material with ternary hybrid nanomaterials. Swarm Evol Comput. 2024;91:101775.

[13] Srilatha P, Kumar RV, Kumar RN, Gowda RP, Abdulrahman A, Prasannakumara BC. Impact of solid-fluid interfacial layer and nanoparticle diameter on Maxwell nanofluid flow subjected to variable thermal conductivity and uniform magnetic field. Heliyon. 2023;9(11):1–18.

[14] Akbar NS, Zamir T, Akram J, Noor T, Muhammad T. Simulation of hybrid boiling nano fluid flow with convective boundary conditions through a porous stretching sheet through Levenberg Marquardt artificial neural networks approach. Int J Heat Mass Transf. 2024;228:125615.

[15] Shamshuddin MD, Salawu SO, Asogwa KK, Rao PS. Thermal exploration of convective transportation of ethylene glycol based magnetized nanofluid flow in porous cylindrical annulus utilizing MOS_2 and Fe_3O_4 nanoparticles with inconstant viscosity. J Magn Magn Mater. 2023;573:170663.

[16] Li D, Li H, Ma L, Lan S. Oscillating flow of Jeffrey fluid in a rough circular microchannel with slip boundary condition. Chin J Phys. 2024;91:107–29.

[17] Alghamdi M, Zamir T, Akbar NS, Muhammad T. Neural intellectual computing systems for the analysis of thermally stratified mixed convective micropolar liquid with the interaction of thermal diffusive nanofluid over a heated sheet. Neural Comput Appl. 2024;37:1–25.

[18] Sun L, Liang T, Zhang C, Chen J. The rheological performance of shear-thickening fluids based on carbon fiber and silica nanocomposite. Phys Fluids. 2023;35(3):1–11.

[19] Abbas N, Shatanawi W, Abodayeh K, Shatnawi TA. Comparative analysis of unsteady flow of induced MHD radiative Sutterby fluid flow at nonlinear stretching cylinder/sheet: Variable thermal conductivity. Alex Eng J. 2023;72:451–61.

[20] Sudarmozhi K, Iranian D, Khan I. Heat and mass transport of MHD viscoelastic fluid flow towards a permeable stretching cylinder. Int Commun Heat Mass Transf. 2023;145:106864.

[21] Khan A, Iqbal Z, Ahammad NA, Sidi MO, Elattar S, Awad S, et al. Bioconvection Maxwell nanofluid flow over a stretching cylinder influenced by chemically reactive activation energy surrounded by a permeable medium. Front Phys. 2023;10:1065264.

[22] Islam S, Khan A, Kumam P, Alrabaiah H, Shah Z, Khan W, et al. Radiative mixed convection flow of maxwell nanofluid over a stretching cylinder with joule heating and heat source/sink effects. Sci Rep. 2020;10(1):17823.

[23] Sowmiya C, Kumar BR. MHD Maxwell nanofluid flow over a stretching cylinder in porous media with microorganisms and activation energy. J Magn Magn Mater. 2023;582:171032.

[24] Ashraf MB, Tanveer A, Ulhaq S. Effects of Cattaneo-Christov heat flux on MHD Jeffery nano fluid flow past a stretching cylinder. J Magn Magn Mater. 2023;565:170154.

[25] Asghar A, Vrinceanu N, Ying TY, Lund LA, Shah Z, Tirth V. Dual solutions of convective rotating flow of three-dimensional hybrid nanofluid across the linear stretching/shrinking sheet. Alex Eng J. 2023;75:297–312.
[26] Alghamdi M, Akbar NS, Zamir T, Muhammad T. Double layered combined convective heated flow of Eyring-Powell fluid across an elevated stretched cylinder using intelligent computing approach. Case Stud Therm Eng. 2024;54:104009.
[27] Madkhali HA, Nawaz M, Alharbi SO. Computational investigation of homogeneous-heterogeneous reactions in fluid with transport mechanisms: a finite element simulations approach. Ain Shams Eng J. 2024;15(3):102449.
[28] Ramzan M, Chaudhry H, Ghazwani HAS, Kadry S, Shahmir N, Abbas M, et al. Impact of homogeneous–heterogeneous reactions on nanofluid flow through a porous channel–A Tiwari and Das model application. Numer Heat Transfer, Part A. 2024;85(8):1317–30.
[29] Naseem A, Shafiq A, Naseem F, Farooq MU. Aspects of homogeneous heterogeneous reactions for nanofluid flow over a riga surface in the presence of viscous dissipation. Energies. 2022;15(19):6891.
[30] He Z, Arain MB, Khan WA, Alzahrani ARR, Muhammad T, Hendy AS, et al. Theoretical exploration of heat transport in a stagnant power-law fluid flow over a stretching spinning porous disk filled with homogeneous-heterogeneous chemical reactions. Case Stud Therm Eng. 2023;50:103406.
[31] Jiang M, Tao X, Chen W, Dai Z. An enhanced interface-sharpening algorithm for accurate simulation of underwater explosion in compressible multiphase flow on complex grids. Phys Fluids. 2025;37(1):1–10.
[32] Shah NA, Koriko OK, Ramesh K, Oreyeni T. Rheology of bioconvective stratified Eyring-Powell nanofluid over a surface with variable thickness and homogeneous-heterogeneous reactions. Biomass Convers Biorefin. 2024;14(17):20823–39.
[33] Kandeal AW, Ismail M, Basem A, Elsayad MM, Alawee WH, Majdi HS, et al. An overview of the improvement of natural convection heat transfer *via* surface thermal radiation for different geometries. Results Eng. 2024;23:102514.
[34] Yang W, Jiang X, Tian X, Hou H, Zhao Y. Phase-field simulation of nano-α′ precipitates under irradiation and dislocations. J Mater Res Technol. 2023;22:1307–21.
[35] Hamad NH, Bilal M, Ali A, Eldin SM, Sharaf M, Rahman MU. Energy transfer through third-grade fluid flow across an inclined stretching sheet subject to thermal radiation and Lorentz force. Sci Rep. 2023;13(1):19643.
[36] Alrehili M. Improvement for engineering applications through a dissipative Carreau nanofluid fluid flow due to a nonlinearly stretching sheet with thermal radiation. Case Stud Therm Eng. 2023;42:102768.
[37] Pandey AK, Bhattacharyya K, Gautam AK, Rajput S, Mandal MS, Chamkha AJ, et al. Insight into the relationship between non-linear mixed convection and thermal radiation: The case of Newtonian fluid flow due to non-linear stretching. Propul Power Res. 2023;12(1):153–65.
[38] Goud BS, Srilatha P, Mahendar D, Srinivasulu T, Reddy YD. Thermal radiation effect on thermostatically stratified MHD fluid flow through an accelerated vertical porous plate with viscous dissipation impact. Partial Diff Equ Appl Math. 2023;7:100488.
[39] Swain K, Ibrahim SM, Dharmaiah G, Noeiaghdam S. Numerical study of nanoparticles aggregation on radiative 3D flow of maxwell fluid over a permeable stretching surface with thermal radiation and heat source/sink. Results Eng. 2023;19:101208.
[40] Kumar MA, Reddy YD. Thermal radiation and chemical reaction influence on MHD boundary layer flow of a Maxwell fluid over a stretching sheet containing nanoparticles. J Therm Anal Calorim. 2023;148(13):6301–9.
[41] Muhammad T, Ullah MZ, Waqas H, Alghamdi M, Riaz A. Thermo-bioconvection in stagnation point flow of third-grade nanofluid towards a stretching cylinder involving motile microorganisms. Phys Scr. 2020;96(3):035208.
[42] Shafiq A, Khan I, Rasool G, Seikh AH, Sherif ESM. Significance of double stratification in stagnation point flow of third-grade fluid towards a radiative stretching cylinder. Mathematics. 2019;7(11):1103.
[43] Ali B, Naqvi RA, Hussain D, Aldossary OM, Hussain S. Magnetic rotating flow of a hybrid nano-materials Ag-MoS_2 and Go-MoS_2 in $C_2H_6O_2$-H_2O hybrid base fluid over an extending surface involving activation energy: FE simulation. Mathematics. 2020;8(10):1730.
[44] Kumari M, Nath G. Transient rotating flow over a moving surface with a magnetic field. Int J Heat Mass Transf. 2005;48(14):2878–85.
[45] Akbar NS, Rafiq M, Muhammad T, Alghamdi M. Electro osmotically interactive biological study of thermally stratified micropolar nanofluid flow for copper and silver nanoparticles in a microchannel. Sci Rep. 2024;14(1):518.